



**HAL**  
open science

# The role of sulfur in molybdenum transport in hydrothermal fluids: Insight from in situ synchrotron XAS experiments and molecular dynamics simulations

Weihua Liu, Barbara Etschmann, Yuan Mei, Qiushi Guan, Denis Testemale, Joël Brugger

## ► To cite this version:

Weihua Liu, Barbara Etschmann, Yuan Mei, Qiushi Guan, Denis Testemale, et al.. The role of sulfur in molybdenum transport in hydrothermal fluids: Insight from in situ synchrotron XAS experiments and molecular dynamics simulations. *Geochimica et Cosmochimica Acta*, 2020, 290, pp.162-179. 10.1016/j.gca.2020.08.003 . hal-03354224

**HAL Id: hal-03354224**

**<https://hal.science/hal-03354224>**

Submitted on 4 Nov 2021

**HAL** is a multi-disciplinary open access archive for the deposit and dissemination of scientific research documents, whether they are published or not. The documents may come from teaching and research institutions in France or abroad, or from public or private research centers.

L'archive ouverte pluridisciplinaire **HAL**, est destinée au dépôt et à la diffusion de documents scientifiques de niveau recherche, publiés ou non, émanant des établissements d'enseignement et de recherche français ou étrangers, des laboratoires publics ou privés.

# 1 The role of sulfur in molybdenum 2 transport in hydrothermal fluids: 3 insight from *in situ* synchrotron 4 XAS experiments and molecular 5 dynamics simulations

6 <sup>1\*</sup>Weihua Liu, <sup>2</sup>Barbara Etschmann, <sup>1</sup>Yuan Mei, <sup>2</sup>Qiushi Guan, <sup>3</sup>Denis Testemale, and  
7 <sup>2</sup>Joël Brugger

8 1. CSIRO Mineral Resources, Clayton, Vic, 3168, Australia

9 2. School of Earth, Atmosphere and Environment, Monash University, Clayton, Vic,  
10 3800, Australia

11 3. Université Grenoble Alpes, CNRS, Grenoble INP, Institut Néel, 38000 Grenoble,  
12 France

13 \*Corresponding author

## 14 Abstract

15 Knowledge of the identity and thermodynamic properties of aqueous molybdenum  
16 species at elevated temperature is important for understanding the extraction of Mo from  
17 source rocks and the formation of hydrothermal deposits. Chlorine and sulfur are two major  
18 components in crustal fluids. Several studies have investigated Mo speciation and solubility  
19 in chloride-bearing hydrothermal fluids, but little is known about the behaviour of Mo in  
20 sulfur-bearing systems at elevated temperature. We used *in-situ* synchrotron X-ray absorption  
21 spectroscopy (XAS) measurements and molecular dynamics (MD) simulations to investigate  
22 the predominant Mo species in S-bearing (0.04-2 m NaHS) solutions at 30-394 °C (XAS) and  
23 77-300 °C (MD) and 800bar. The XAS data show that, similar to previous room temperature  
24 studies, the S<sup>2-</sup> ion progressively replaces O<sup>2-</sup> in molybdate (MoO<sub>4</sub><sup>2-</sup>) to form thiomolybdates  
25 (MoO<sub>4-x</sub>S<sub>x</sub><sup>2-</sup>, x = 1, 2, 3, 4) with increasing NaHS concentrations at temperature up to 394 °C.  
26 The MD simulations confirm the identity and structure of the thiomolybdate species

27 determined from the XAS experimental data. The speciation calculations based on the  
28 formation constants for the thiomolybdate species extrapolated from the room temperature  
29 data agree well with the experimental results. This study indicates that thiomolybdate species  
30 are likely to be important in transporting Mo in sulfur-bearing, weak-acidic to alkaline,  
31 hydrothermal fluids under reduced (sulfide stable) conditions in the Earth crust. Current  
32 models of Mo transport in hydrothermal ore fluids need to be re-evaluated to take into  
33 account the thiomolybdate species.

## 34 1. Introduction

35 Molybdenum (Mo) is mainly mined from magmatic hydrothermal deposits (e.g.,  
36 porphyry Cu-Mo-Au deposits), where the metals including Mo are transported in high  
37 temperature-pressure geological fluids and deposited to form ores under favourable  
38 physiochemical conditions (e.g., [Seedorff et al., 2005](#)). Molybdenum is also enriched in other  
39 hydrothermal systems, including IOCG deposits (e.g., Olympic Dam, South Australia, [Ehrig  
40 et al. 2012](#); Uranium roll-front deposits, [Bonnetti et al. 2020](#); [Bullock and Parnell 2017](#)).  
41 Furthermore, elevated molybdenum concentrations are also found in sedimentary rocks such  
42 as shales, and Mo is commonly used as a paleoredox indicator (e.g., [Asael et al. 2018](#); [Tessin  
43 et al. 2018](#)). Therefore, the identity and thermodynamic properties of the aqueous Mo species  
44 prevalent in crustal fluids are important for understanding the formation of hydrothermal Mo  
45 deposits and constrain the use of molybdenum as a geological tracer.

46 A number of experimental and theoretical studies have investigated Mo speciation  
47 and solubility in hydrothermal fluids, and the partitioning of Mo between melt, vapour and  
48 aqueous phases (e.g., [Candela and Holland 1984](#), [Dadze et al. 2017, 2018](#); [Keppler and  
49 Wyllie, 1991](#); [Kudrin, 1989](#), [Rempel, et al., 2006, 2008, 2009](#); [Ulrich and Mavrogenes, 2008](#),  
50 [Zajacz et al., 2017](#)). These studies suggest that Mo(VI) species predominate under a wide  
51 range of redox conditions from oxidised to MoO<sub>3</sub>(s)/MoO<sub>2</sub>(s) stable conditions. In pure  
52 water, the hydrogen molybdate (HMoO<sub>4</sub><sup>-</sup>) and molybdate (MoO<sub>4</sub><sup>2-</sup>) ions are thought to be  
53 dominant, and their ionization constants were determined up to 300 °C by [Minubayeva and  
54 Seward \(2010\)](#); molybdic acid, H<sub>2</sub>MoO<sub>4</sub>(aq), predominates only under highly acidic  
55 conditions, especially at T>100 °C ([Borg et al. 2012](#)). Recently, [Dadze et al. \(2017\)](#) obtained  
56 the solubility constants for crystalline MoO<sub>3</sub>(s) in acidic solutions up to 350 °C as  
57 H<sub>2</sub>MoO<sub>4</sub>(aq) and HMoO<sub>4</sub><sup>-</sup>, and [Saha et al. \(2017\)](#) used a hydrothermal diamond anvil cell to

58 measure MoO<sub>2</sub>(s) solubilities in pure water of 44 ppm and 658 ppm at 600 and 800 °C,  
59 respectively; however, they were not able to determine the oxidation state and predominant  
60 Mo species in the solutions. In pure, low density water vapour, a neutral MoO<sub>3</sub>(H<sub>2</sub>O)<sub>n</sub>(aq)  
61 with hydration number n up to 3 at 360 °C was proposed based on the solubility of MoO<sub>3</sub>(s)  
62 (Rempel et al. , 2006).

63 The structures of the molybdate and hydrogen molybdate ions show little change with  
64 increasing temperature, as evidenced by the synchrotron X-ray absorption study (up to  
65 385 °C) of Borg et al. (2012); both species share a tetrahedral coordination, and confirmed by  
66 the *first principle* molecular simulations study of Liu et al. (2013). Liu et al. (2013) also  
67 predicts the change of the structure of molybdic acid from 6-coordinated MoO<sub>2</sub>(OH)<sub>2</sub>  
68 (H<sub>2</sub>O)<sub>2</sub>(aq) to 4-coordinated, unhydrated MoO<sub>2</sub>OH<sub>2</sub>(aq) with increasing temperatures to 300  
69 °C. They calculated the acidity constants of molybdic acid up to 300 °C with reasonably good  
70 agreement with the experimental results by Minubayeva and Seward (2010), in particular for  
71 pKa1.

72 The possibility of Mo(VI) complexation with chloride, the major ligand in many  
73 hydrothermal fluids, has also been investigated. Wood et al. (1987) noted that Mo did not  
74 complex with chloride in their slightly acidic (pH>3) chloride-bearing experimental solutions  
75 (0-5 m NaCl, 25-350 °C), and Kurin (1989) proposed that KHM<sub>4</sub>O<sub>4</sub>(aq) and NaHM<sub>4</sub>O<sub>4</sub>(aq)  
76 are responsible for the Mo solubility in 0.05-1 m KCl and NaCl solutions (with 0.1 m HCl to  
77 0.005 m KOH) at 300-394 °C. Under much more acidic conditions, Borg et al. (2012)  
78 identified oxo-chloro complexes MoO<sub>m</sub>Cl<sub>n</sub><sup>6-2m-n</sup> (n up to 5) at the experimental P-T conditions  
79 (up to 385°C at 600 bar), consistent with the solubility study by Dadze et al. (2018), in which  
80 they found MoO<sub>2</sub>(OH)<sub>2</sub>Cl<sup>-</sup> predominant in HCl-HClO<sub>4</sub>-NaCl solutions at 300 °C. In HCl-  
81 bearing vapour phase, hydrated species MoO<sub>3</sub>(H<sub>2</sub>O)<sub>y</sub>(g) predominate in less acidic vapour  
82 (log<sub>f</sub><sub>HCl(g)</sub> < 0.1, Hurtig and Williams-Jones, 2014) and MoO<sub>2</sub>Cl<sub>2</sub>(g) is dominant in more  
83 acidic conditions (Rempel et al., 2008).

84 Sulfur is one of the major components in magmatic hydrothermal fluids and volcanic  
85 gases, and molybdenite, MoS<sub>2</sub>, is the main form of Mo in ore deposits. Recent experimental  
86 and theoretical studies have shown that sulfur complexes with ore metals, and can be an  
87 important transport agent for Au, Cu, Zn and Pd (Pokrovski et al., 2009, Etschmann et al.,  
88 2010, 2019, Mei, 2013, 2015 2016; Liu et al., 2014; Brugger et al. 2016). Therefore, it is  
89 desirable to investigate the complexation between Mo and S and it's contribute to Mo

90 transport in hydrothermal fluids. Most previous studies of the hydrothermal transport of Mo  
91 focused on Mo speciation in pure water and chloride-bearing systems, with much less work  
92 on the behaviour of Mo in hydrothermal sulfur-bearing fluids. Wood et al. (1987) didn't find  
93 evidence of Mo-S species in their multi-metal solubility experiments in 0-5 molal NaCl  
94 solution with pyrite-pyrrhotite-magnetite buffer for  $\log fO_2$  and  $\log fS_2$  at 200-350 °C and  
95 0.69-172 bar, whereas Zhang et al. (2012) suggests  $NaHMoO_2S_2$  predominant in their  
96 experimental solutions at 600-800 °C and 2000 bar, but find the solubility of  $MoS_2$  increases  
97 with decreasing  $\log fS_2$ .

98 Under the ambient condition, Mo(VI)-S species or thiomolybdates have been  
99 suggested to be important in sediment and surface water environments (e.g., [Helz et al., 1996](#),  
100 [Erickson and Helz, 2000](#)). Thiomolybdate anions ( $MoO_{4-x}S_x^{2-}$ ,  $x = 1, 2, 3, 4$ ) have been studied  
101 extensively with different methods (see reviews by [Muller et al., 1981](#); [Coucovanis, 1998](#);  
102 [Laurie, 2000](#); and [Smedley and Kinniburgh, 2017](#)). The kinetics and reaction constants of  
103 progressive replacement of oxygen by sulfur was established using mainly UV-Vis  
104 spectrophotometry (e.g., [Harmer and Sykes, 1980](#); [Erickson and Helz, 2000](#)) and theoretical  
105 studies (e.g., [Bernholc and Stiefel, 1985](#), [El-Issa et al., 1989](#), [Tossell, 2005](#)). These studies  
106 generally agree that thiomolybdate species are important in surface waters under reduced  
107 environments. In contrast to detailed information available at room temperature, the identity  
108 and stability of the thiomolybdates in hydrothermal fluids at elevated temperature and  
109 pressure remain unknown. Furthermore, the thiomolybdate anion notably tends to form stable  
110 complexes with some transition metal ions such as Cu(I) ([Helz et al., 2011](#)) and Fe(II)  
111 ([Helz et al., 1996, 2014](#)) at room temperature, indicating the potential for co-transport of Fe  
112 and Cu with Mo in reduced, sulfur-rich fluids.

113 This work aimed to determine the speciation of Mo(VI) in hydrosulfide solutions at  
114 elevated temperature and pressure (up to 394 °C and 800 bar). We used *in-situ* Extended X-  
115 ray Absorption Fine Structure (EXAFS) spectroscopy and X-ray Absorption Near-edge  
116 Structure (XANES) data to obtain structural information for the predominant Mo species,  
117 combined with *ab initio* molecular dynamics simulations and *ab initio* XANES calculations  
118 to provide new insights for Mo transport and deposition in natural and engineered  
119 hydrothermal fluids relevant to the hydrothermal (re)mobilisation of Mo and formation of Mo  
120 deposits, as well as the hydrometallurgical processing of Mo-bearing ores.

## 121 2. Methods

### 122 2.1. XAS experiment

#### 123 2.1.1. Sample solutions

124 All sample solutions were prepared from deionized water,  $\text{Na}_2\text{MoO}_4 \cdot 2\text{H}_2\text{O}$ (s)  
125 (analytical grade, Sigma Aldrich™) and a stock of 2 m NaHS solution. The NaHS stock  
126 solution was prepared by dissolving sodium hydroxide in deoxygenated water, and then  
127 bubbling  $\text{H}_2\text{S}$ (g) through the solution. This method was used by [Helz et al. \(1993\)](#),  
128 [Mosselmans et al. \(1999\)](#), [Etschmann et al. \(2010\)](#) and [Mei et al. \(2016\)](#) for studies on Cu(I)  
129 and Zn(II) bisulfide complexes, and it was demonstrated that the oxidation state of the sample  
130 solutions (loaded in glassy carbon cells) were within the stability field of the reduced sulfur  
131 over a large temperature range (up to 592 °C) ([Etschmann et al., 2010](#)). The solution  
132 compositions are compiled in [Table 1](#).

#### 133 2.1.2. Sample cell and XAS measurement

134 Molybdenum K-edge (20,000 eV) X-ray Absorption Near Edge Structure (XANES)  
135 and Extended X-ray absorption Fine Structure (EXAFS) spectra were measured at beamline  
136 30-BM (FAME) at the European Synchrotron Radiation Facility (ESRF) in Grenoble, France.  
137 The setup at the FAME beam line has been described by [Proux et al. \(2005\)](#). A focused beam  
138 size of FWHM  $300 \times 150 \mu\text{m}^2$  was used. The incident and transmitted beam intensity  $I_0$  and  
139  $I_1$  were measured with Si diodes; and fluorescence data were collected concurrently using a  
140 30 element solid state fluorescence detector. The beam energy was calibrated with a Mo foil,  
141 such that the maximum of the first derivative of the XANES spectrum was at 20,000 eV.

142 The high temperature-high pressure cell developed by the “Laboratoire de  
143 Cristallographie” (CNRS) was used for XAS measurements of solutions up to supercritical  
144 conditions ([Testemale et al., 2005](#)). The cell consists of an external water-cooled high-  
145 pressure vessel equipped with three 1.5 mm thick beryllium windows enabling collection of  
146 fluorescence and transmission signals at a pressure of 800 bar. A sample solution (mass  
147  $\sim 0.1$  g) was contained inside a glassy carbon tube with an internal diameter of 4 mm. The  
148 pressure was applied to the sample by two glassy carbon pistons, using helium as a pressure  
149 medium. The glassy carbon tube was placed inside a small cylindrical resistive heater; the  
150 heater and tube are installed inside in a water-cooled stainless-steel high-pressure vessel. The  
151 temperature of the fluid at the beam location was controlled by a Eurotherm PID controller to

152 a stability within 0.1 °C, and calibrated by correlating the density of a 2 molal NaCl solution  
153 at the beam position as a function of temperature, based on measurements of X-ray  
154 transmission (e.g., [Tooth et al., 2013](#)):

$$\mu_{20\text{keV}}^{\text{AGS}} - \mu_{20\text{keV}}^{\text{AGS}} = \left( \frac{\mu}{\rho} \right)_{20\text{keV}}^S \rho^S x$$

155  
156 (1),

157 where  $\mu_{20\text{keV}}^{\text{AGS}}$  is the measured transmission of the autoclave + glassy carbon cell + 800 bar He  
158 + solution at 20 keV,  $\mu_{20\text{keV}}^{\text{AGS}}$  is the measured baseline transmission without solution,  $\left( \frac{\mu}{\rho} \right)_{20\text{keV}}^S$  is  
159 the tabulated X-ray mass attenuation coefficient corresponding to the composition of solution  
160  $S$  at 20 keV (Chantler, 1995),  $\rho^S$  is the density of the solution (program Sowat, [Driesner,](#)  
161 [2007; Driesner and Heinrich, 2007](#)), and  $x$  is the path length of the beam in the solution. The  
162 error from the calibration curve is  $\sim \pm 3$  °C. The details of the autoclave can be found in  
163 several previous studies (e.g., [Testemale et al., 2005; 2009; Liu et al., 2011; Tooth et al.](#)  
164 [2013](#)).

165 XANES and EXAFS data were analysed with the HORAE package ([Ravel and](#)  
166 [Newville, 2005](#)), using FEFF version 9 ([Rehr et al., 2009](#)). The reported errors are at the 1<sup>o</sup>  
167 level and taken from the HORAE package.

## 168 2.2. *Ab initio* molecular dynamics simulations

169 The simulations of molybdic acid, molybdates and thiomolybdates were performed  
170 with solutions containing 1 H<sub>2</sub>MoO<sub>4</sub>, 4 Na<sup>+</sup>, 4 HS<sup>-</sup> and 111 H<sub>2</sub>O to represent Na and S  
171 concentrations of 2 molal. The nominal Mo concentration is 0.5 molal, but because there is  
172 only one Mo atom in the simulation box, there is no Mo-Mo interaction, i.e. Mo behaves as if  
173 at infinite dilution in the simulated solutions. Periodic boundary conditions were applied in  
174 the *ab initio* MD simulations. We performed simulations at 77 °C, 200 °C and 300 °C at  
175 800 bar to compare with the XAS experiments, and at near-saturation pressure at 200 °C  
176 (20 bar) and 300°C (100 bar). The simulations were run in the NVT ensemble with the  
177 temperature controlled by the Nosé thermostat for both the ions and electrons ([Nosé, 1984,](#)  
178 [Hoover, 1985](#)). For these constant volumes calculations, the densities were taken from the  
179 equations ofstate of a 2 molal NaCl solution ([Driesner, 2007; Driesner and Heinrich, 2007](#)),

180 an approximation that has been widely used in hydrothermal aqueous geochemical systems.  
181 Details of the physical conditions for each simulation are listed in [Table 2](#). To test the  
182 stability of molybdic acid and thiomolybdates, simulations with six different initial species,  
183 i.e.,  $\text{H}_2\text{MoO}_4$ ,  $\text{MoO}_4^{2-}$ ,  $\text{MoO}_3\text{S}^{2-}$ ,  $\text{MoO}_2\text{S}_2^{2-}$ ,  $\text{MoOS}_3^{2-}$   $\text{MoS}_4^{2-}$ , were conducted at each T-P  
184 condition, for a total of 25 simulations

185 *Ab initio* molecular dynamics simulations were performed using the  
186 CP2K/QUICKSTEP package, which implements density functional theory (DFT) using a  
187 mixed Gaussian basis sets and plane-waves approach ([Hutter et al., 2014](#)). Goedecker-Teter-  
188 Hutter (GTH) pseudopotentials ([Goedecker et al., 1996](#); [Hartwigsen et al., 1998](#)) were used  
189 for the core electrons with a cutoff of 280 Ry (3809.6 eV) for the electron density, and the  
190 double-zeta valence polarized (DZVP) basis sets were utilised for Mo, Na, S, O and H  
191 ([VandeVondele and Hutter 2007](#)) together with BLYP exchange-correlation functional ([Lee](#)  
192 [et al., 1988](#); [Becke, 1988](#)). The BLYP functional generally provides a good description of the  
193 structural properties of water including O–O interactions, H-bond statistics, angular  
194 distributions, coordination numbers, and radial distribution functions when compared with  
195 experiments ([Gillan et al., 2016](#); [Lin et al., 2012](#)). However, as discussed in our previous  
196 studies using the BLYP exchange correlation functional ([Mei et al., 2018](#); [Guan et al., 2020](#)),  
197 we note that there is a well-known tendency for most functionals, including BLYP, to over-  
198 structure liquid water ([Lee and Tuckerman, 2006](#); [Lin et al., 2012](#)). For example, [Bankura et](#)  
199 [al. \(2014\)](#) showed that BLYP, like most other functionals, best reproduces the hydrogen-  
200 bonded network of water at ambient conditions when using an elevated temperature (80 °C in  
201 their case), and it could be argued that there is a temperature offset of approximately 50-  
202 55 °C between the computed data as compared to the experimental structure of the solvent at  
203 room temperature. Therefore, here we performed simulations at 77 °C (350K) to reproduce  
204 the solution at room temperature. A simulation timestep of 0.5 femtosecond (fs,  $10^{-15}$  second)  
205 was chosen for all simulations. To achieve **good statistics**, all the simulations were calculated  
206 for 9-15 ps including a 2 ps equilibration. The radial distribution functions (RDF) and the  
207 coordination number (integrals of RDF) were calculated using VMD ([Humphrey et al., 1996](#))  
208 to extract the averaged structural information and to compare with the XAS data. As  
209 discussed previously (e.g., [Mei et al., 2020](#)), *ab initio* MD simulations are computationally  
210 intensive. *Ab initio* MD studies published by researchers from various groups ([Jahn and](#)  
211 [Schmidt, 2010](#); [Sulpizi et al., 2013](#); [Liu et al., 2013a, b](#); [Wagner et al., 2017](#); [Stefanski and](#)



212 [Jahn 2020](#)) indicate that it is viable to represent the geometrical and thermodynamic  
213 properties of solute and solvent molecules within manageable simulation times of tens of  
214 picoseconds.

### 215 2.3. *Ab initio* XANES calculations

216 *Ab initio* XANES spectra were calculated with the FDMNES program ([Joly, 2001](#)).  
217 The final states were calculated by the Finite Difference Method (FDM) to solve the  
218 Schrodinger equation in the cluster. The FDM can provide accurate calculation especially for  
219 structure of low-symmetry aqueous complexes ([Joly, 2001](#); [Brugger et al., 2007](#)), as in this  
220 study. To compare with the experimental spectra, the calculated spectra were convoluted with  
221 a Lorentzian function of energy-dependent width to account for the core-hole lifetime  
222 broadening (4.52 eV; [Krause and Oliver, 1979](#)) and the inelastic plasmon interactions with  
223 the photoelectron. The energy resolution of the monochromator was taken into account by  
224 convoluting the calculated XANES spectra with a Gaussian function (width of 1.024 eV). We  
225 also calculated the XANES spectra of the five Mo-O-S complexes simulated with molecular  
226 dynamics ( $\text{MoO}_{4-x}\text{S}_x^{2-}$ ,  $x = 0-4$ ) at 77 and 300 °C. 40 frames were chosen at every 0.2 ps from  
227 each MD simulation box and the final spectra were obtained by taking the average of  
228 FDMNES simulations of the 40 frames. The radius cutoff of all calculations was 5 Å.

## 229 3. Results

230 Molybdenum K-edge XANES and EXAFS spectra for the sample solutions with  
231 variable NaHS concentrations between 0.07 to 2 molal (Table 1) were collected between 30-  
232 394 °C at 800 bar, as well as the spectra of molybdenum reference compounds, including the  
233 molybdate solution for comparison. In general, the data collected from the solution are of  
234 good quality for EXAFS analysis at temperature up to 286-330 °C, and then only XANES  
235 data are used at higher temperatures up to the maximal temperature values for each solution  
236 listed in Table 1. At higher temperatures than the maximal temperatures, the intensity of the  
237 spectra dropped dramatically, and the signal become noisier due to a reduced metal solubility  
238 and precipitates on the wall of the cell, as a result of the decrease in solution density (e.g.,  
239 Pokrovski et al. 2005; Liu et al. 2008; Mei et al. 2014). Most spectra of precipitates are too  
240 noisy to identify, but the spectrum of the highest NaHS concentrations (Sol6) has similarity  
241 with the spectrum of molybdenite ( $\text{MoS}_2$ ) (see insert in Fig. 1b); therefore, the precipitates  
242 are likely to be molybdenite. For all the samples, only the good quality XANES and EXAFS  
243 of the solution phase are used in the data analysis.

244 In the following sections we describe the qualitative analysis of the XANES spectra,  
245 followed by the quantitative refinement of the EXAFS data for the determination of the  
246 coordination structure (bond distance, ligand types and coordination numbers) and  
247 predominating species. The results of the molecular dynamics simulations and XANES  
248 calculations of the major Mo-O and Mo-S species are then described and compared with the  
249 experimental results.

### 250 3.1. XANES

251 *Effect of NaHS concentration:* The XANES spectra of sample solutions as a function  
252 of NaHS concentration at 30 and 286 °C are plotted in Fig. 1a and 1b respectively, together  
253 with the spectra of two end-member references,  $\text{Na}_2\text{MoO}_4$  solid (containing the  $[\text{MoO}_4]^{2-}$   
254 moiety – we use [ ] to refer to the moiety of a species throughout the text) and  $(\text{NH}_4)_2\text{MoS}_4$  (s)  
255 (containing the  $[\text{MoS}_4]^{2-}$  moiety). The spectra of the sample solutions plot between the spectra  
256 of these two references, with the dominant absorbing species in the sample solutions evolving  
257 from  $[\text{MoO}_4]^{2-}$ -like to  $[\text{MoS}_4]^{2-}$ -like structures with increasing bisulfide concentration. The  
258  $[\text{MoO}_4]^{2-}$  structure has a distinctive pre-edge peak at ~20,005 eV (Feature A), which is  
259 associated with the 1s – 4d transition, and related to (i) the number of Mo=O bonds per Mo  
260 atom and (ii) the symmetry of the structure, the more symmetrical structures having a smaller

261 pre-edge (Borg et al., 2012 and references therein). The pre-edge peak of the spectrum of the  
262  $[\text{MoS}_4]^{2-}$  moiety at 20,003 eV is smaller than that of the  $[\text{MoO}_4]^{2-}$  moiety at 20,005 eV  
263 (Fig. 1a). At both temperatures (30 and 286 °C), the pre-edge feature decreases with  
264 increasing NaHS concentration, indicating an increased contribution of the  $[\text{MoS}_4]^{2-}$ -like  
265 species. The features B, C, and D also show systematic changes as a function of NaHS  
266 concentration, consistent with the features of the two end-member spectra.

267 *Effect of increasing temperature.* Temperature has a smaller effect on the XANES  
268 spectra than  $\text{HS}^-$  concentration (Fig. 2). The spectral changes with increasing temperatures  
269 are mainly reflected in the growing pre-edge peak (feature of the  $[\text{MoO}_4]^{2-}$  moiety) with  
270 increasing temperature for most solutions (except for low NaHS solutions such as Sol14 and  
271 Sol12), indicating increased contribution from  $[\text{MoO}_4]^{2-}$  with increasing temperature.

### 272 3.2. EXAFS

273 The changes of the EXAFS spectra as a function of NaHS concentration (Fig. 3) are  
274 similar to the trend of the XANES spectra. In particular, the (phase uncorrected) Fourier  
275 transform of the EXAFS shows a decreasing intensity of the first peak at  $\sim 1.3$  Å and  
276 increasing intensity of the second peak at  $\sim 1.8$  Å (Fig. 3) with increasing NaHS  
277 concentration. Quantitative EXAFS refinements (Table 3) reveal that the first peak is due to  
278 Mo-O interaction and the second peak is due to Mo-S.

279 EXAFS refinement of a molybdate standard ( $\text{Na}_2\text{MoO}_4(\text{s})$ ) containing the  $[\text{MoO}_4]^{2-}$   
280 moiety) indicates 4 oxygen around Mo atom at average distance of 1.775(4) Å, similar to the  
281 Mo-O distance in molybdate solution (1.771-1.777 Å, Borg et al. 2012). The EXAFS  
282 refinement of the  $(\text{NH}_4)_2\text{MoS}_4(\text{s})$  reference compound ( $[\text{MoS}_4]^{2-}$  moiety) yields an average  
283 Mo-S bond distance of 2.192(5) Å. This value is similar to the published individual Mo(VI)-  
284 S bond distances in  $[\text{MoS}_4]^{2-}$  moiety determined by EXAFS refinements (2.20 Å in  
285  $(\text{NH}_4)_2\text{MoS}_4(\text{s})$ , Bostick et al., 2003; 2.18 Å in  $\text{MoS}_4^{2-}$  solution, Dahl et al, 2013) and by  
286 single crystal diffraction (2.1773(5) -2.2013(8) Å in  $(\text{NH}_4)_2\text{MoS}_4(\text{s})$ ; average = 2.1844(6) Å;  
287 Hill et al., 2010). The fitted bond distance of the Mo-S bonds for solutions S5 and S6 with  
288 the highest NaHS concentrations, where the Mo-S peaks are most significant (Fig. 4), are also  
289 around 2.20 -2.21 Å at 30°C (Table 3); however, the refined Mo-S bond distances of  
290 solutions with a low concentration of NaHS and higher temperatures have longer distances of  
291  $\sim 2.25$ -2.29 Å (Table 3). This is due in part to the larger uncertainties in Mo-S distance  
292 because of the lower number of coordinated S, but also reflects the effect of the dominating

293 Mo-O bond. This is confirmed by the molecular dynamics simulations that indicate slightly  
294 longer (0.02-0.03 Å) Mo-S distances at elevated temperatures for mixed Mo-S and Mo-O  
295 species (See section 3.3).

296 The fitted number of S ligands increases with increasing NaHS concentrations at all  
297 temperatures, at the expense of the number of O atoms, reflecting an increased contribution  
298 from thio species (Table 3; the examples at 30 and 286 °C are plotted in Fig. 5). At the  
299 highest NaHS concentration (Sol6), the fitted number of S ligands is 3.1(2) at 30 °C; with  
300 increasing temperature to 200 °C, the S ligand number increases to 3.4, but at 286 °C and  
301 higher temperature, the S peak decreases notably and the O peak increases (Fig. 3b); this  
302 reflects an increase in O ligand numbers at those temperatures relative to lower temperatures  
303 (Table 3). The temperature dependence of the EXAFS spectra is consistent with, but more  
304 apparent than the change of the pre-edge feature in the XANES (Fig. 2). It is notable that  
305 while EXAFS analysis provides the average numbers of S and O ligands, it cannot  
306 distinguish explicitly the identity of the species present, i.e., for an equal ratio of S:O ligands  
307 obtained from the EXAFS refinement, it is not possible to tell whether it is 1:1 mixture of  
308  $\text{MoO}_4^{2-}$  and  $\text{MoS}_4^{2-}$ , or predominantly a mixed ligand complex such as  $\text{MoS}_2\text{O}_2^{2-}$ .

### 309 3.3. *Ab initio* MD

310 The results of simulations of Mo(VI) speciation in solutions containing 2 m NaHS==  
311 at experimental pressures (800 bar) and at near saturation pressure (200 °C, 20 bar and  
312 300 °C, 100 bar) are listed in Table 4. Overall, the simulations show that fourfold tetrahedral  
313 complexes are stable in all simulations. Apart from some deprotonation for simulations that  
314 started with  $\text{H}_2\text{MoO}_4(\text{aq})$ , no ion exchange was observed during the simulation (up to 25 ps).  
315 Our previous studies show that in the MD simulations on the scale of picoseconds, it is  
316 difficult to observe simple ligand exchange between ions with charge of -1 such as  $\text{Cl}^-$ ,  $\text{HS}^-$   
317 and  $\text{OH}^-$  due to the slow exchange kinetics even at elevated temperatures (Mei et al. 2015,  
318 2016, 2020).

#### 319 3.3.1. Molybdate and hydrogen molybdate ions

320 As shown in Table 4, jobs 1A, 2A, 3A, 4A, 5A that started with  $\text{H}_2\text{MoO}_4(\text{aq})$   
321 established that the hydrogen molybdate ion,  $\text{HMoO}_4^-$ , was the predominant species over the  
322 entire temperature range, with a minor amount of  $\text{H}_2\text{MoO}_4(\text{aq})$  at 77 °C (representing room  
323 T), 800 bar and a minor amount of molybdate ion,  $\text{MoO}_4^{2-}$ , at 300 °C, 100 bar. The molybdate

324 ion is stable in most of the simulations that started with  $\text{Na}_2\text{MoO}_4$  (simulation 6-11, Table 4),  
325 except one solution (simulation 11) at 300 °C in which the stable species is  $\text{HMoO}_4^-$ .  
326 Snapshots of the structures for the observed molybdate and hydrogen molybdate ions are  
327 shown in Fig. 6. The Mo-O distance in  $\text{MoO}_4^{2-}$  is  $\sim 1.80(3)$  Å at 77 °C, which is consistent  
328 with Liu (2013)'s values of 1.79 Å for Mo-O distance in  $\text{MoO}_4^{2-}$ . For  $\text{HMoO}_4^-$ , our MD  
329 results show that the Mo-OH bond distances ( $\sim 1.92$ - $1.94$  Å) are notably longer than the Mo-  
330 O distances ( $\sim 1.77$  Å) (Table 4), also similar to the previous MD results ( $d_{\text{Mo-O}} = 1.76$  Å and  
331  $d_{\text{Mo-OH}} = 1.79$  Å, Liu et al., 2013a;  $d_{\text{Mo-O}} = 1.72$  Å and  $d_{\text{Mo-OH}} = 1.8$  Å, Zhang et al., 2018).  
332 Fig. 7 shows the radial distribution functions (RDF) and the coordination numbers (CN;  
333 integral of RDF) of Mo-O/S at 300 °C, 800 bar. For simulation 5A, where  $\text{HMoO}_4^-$  is the  
334 predominant species, the RDF peak ranges from 1.7 – 2.0 Å (blue solid line) reflecting the  
335 Mo-O bond, which was split into one large peak at 1.77 Å and one small peak at 1.92 Å. The  
336 CN (dashed blue) curve shows the first peak results in a CN of 3 (corresponding to three Mo-  
337 O bonds) and the second peak adds one more ligand (corresponding to one Mo-OH bond),  
338 with a total CN of four. The simulated Mo-O bond distances for molybdate are also  
339 consistent with the experimental EXAFS results for molybdate ( $d_{\text{Mo-O}} = 1.771$ - $1.777$  Å, Borg  
340 et al., 2012;  $1.775(4)$  Å, this study).

### 341 3.3.2. Thiomolybdates

342 All simulations of thiomolybdates show that fourfold tetrahedral complexes are  
343 stable. The geometrical properties of all MD runs are listed in Table 4. Fig. 8 shows the  
344 snapshots of thiomolybdates ( $\text{MoO}_{4-x}\text{S}_x^{2-}$ ,  $x = 1, 2, 3, 4$ ) calculated at 300 °C, 800 bar from  
345 MD simulations. As shown in Table 4, the Mo-O and Mo-S bonds are easily distinguishable  
346 by their lengths ( $\sim 0.45$  Å difference), with Mo-O distances of 1.78-1.79 Å and Mo-S  
347 distances of 2.23-2.28 Å. This is reflected in the RDF plot (Fig. 7), consistent with the  
348 systematic change of Mo-O and Mo-S peaks in the Fourier transforms of the EXAFS data  
349 (Figs. 3, 4), and the bond distances from the MD simulations agree well with the fitted  
350 EXAFS results of Mo-S distances of 2.20-2.3 Å (Table 3). In particular, both the EXAFS  
351 refinements and the MD results predict slightly longer (0.02-0.05 Å) Mo-S distances at  
352 elevated temperatures for mixed thiomolybdates ( $\text{MoO}_{4-x}\text{S}_x^{2-}$ ,  $x = 1, 2, 3$ ). This may indicate  
353 that temperature favours the loosening of the Mo-S bond in the mixed species.

354 Similar to the simulations for molybdates, no ligand exchange or proton exchange  
355 was observed during these simulations. As mentioned before, ligand exchange is unlikely to  
356 be observed in such short simulation times, and in this case, it is even more difficult to see the  
357 exchange between  $O^{2-}$  and  $S^{2-}$  given their strong affinity with  $Mo^{6+}$  due to their differences in  
358 electronegativity. The MD results shown here provide geometrical properties of  
359 thiomolybdates for *ab initio* XANES calculations and provide an independent check and  
360 comparison with EXAFS data.

### 361 3.4. *Ab initio* XANES calculations

362 The XANES spectra calculated using FDMNES and selected experimental spectra are  
363 plotted in Fig. 9. Although the peaks in the experimental spectra are broader than the  
364 calculated spectra, the major spectral features observed in the experimental data are  
365 confirmed by *ab initio* XANES simulations. As shown in Fig. 9, the pre-edge peak  
366 (Feature A) has a slight shift to higher energy (blue shift) when the structure changes from  
367  $[MoS_4]^{2-}$  to  $[MoO_4]^{2-}$ , with increased intensity for the  $[MoO_4]^{2-}$  structure. The peak (Feature  
368 B) that is prominent in the spectrum of the  $[MoS_4]^{2-}$  moiety decreases with decreasing the  
369 number of S ligand and is absent in the spectrum of the  $[MoO_4]^{2-}$  structure. These features are  
370 consistent with the experimental XANES spectra of the two end member references and the  
371 sample solutions (Fig. 9), though the after-edge features C and D in the experimental spectra  
372 are not reproduced in the XANES simulations. The spectral changes from 77 °C to 300 °C  
373 are minimal, confirming the rigid structure of the thiomolybdate structures.

## 374 4. Discussions and conclusions

### 375 4.1. Comparison to previous studies at room temperature

376 It has long been documented that thiomolybdate species are important in surface  
377 environments (Muller et al., 1981; Coucouvanis, 1998; Laurie, 2000). Our results from  
378 EXAFS analysis, *ab initio* MD simulations and XANES calculations confirmed the formation  
379 of thiomolybdates in reduced sulfur-bearing solutions. Several UV-Vis spectroscopic studies  
380 (e.g., Harmer and Sykes, 1980; Erickson and Helz, 2000) suggest that thiomolybdate anions  
381 prevail in reduced sulfur-bearing fluids, and have established the kinetics of stepwise  
382 replacement of  $O^{2-}$  ions by  $S^{2-}$ . In particular, Erickson and Helz's (2000) UV-Vis study  
383 provided the formation constants of the thiomolybdates, and proposed that a sharp transition

384 occurred between  $\text{MoO}_4^{2-}$  to  $\text{MoS}_4^{2-}$ , where a 3-fold change in  $\text{H}_2\text{S}$  concentration results in a  
385 100-fold change in the  $\text{MoO}_4^{2-}/\text{MoS}_4^{2-}$  ratio, and  $\text{MoS}_4^{2-}$  becomes predominant in the solution.  
386 In our experiment we identified a mixture of  $\text{MoO}_4^{2-}$  and  $\text{MoS}_4^{2-}$  in the most solutions, with  
387 the  $\text{MoS}_4^{2-}$  predominant in the high NaHS concentration solutions. The fitted maximum S  
388 ligand number is 3.4 in the 2 m NaHS solution at 200 °C (Table 3). We did not observe 100%  
389  $\text{MoS}_4^{2-}$  in any solutions, as we were not able to prepare a sufficiently concentrated solution,  
390 due to the precipitation of  $\text{MoS}_2$ , for XAS measurement at the lower pH (6-8) where  $\text{MoS}_4^{2-}$   
391 would be more predominant as shown in the previous studies at room temperatures (e.g.,  
392 Erickson and Helz, 2000),

393 Using the formation constants for the  $\text{MoO}_{4-x}\text{S}_x^{2-}$  ( $x = 1, 2, 3, 4$ ) species determined by  
394 Erickson and Helz (2000) and the thermodynamic properties of molybdate species  
395 (Minubayeva and Seward, 2010) and molybdenite by Robie and Hemingway (1995), we  
396 calculated the stability fields of predominant Mo species in a solution of 0.01 m Mo and  
397 0.1 m total sulfur at 25 °C (Fig. 10a). Under reduced conditions, molybdenite predominates in  
398 solutions with a wide range of pH, and molybdate species under more oxidised conditions;  
399 which is contradictory to the thiomolybdate species observed in our experiments and previous  
400 UV-Vis studies (e.g., Harmer and Sykes, 1980; Erickson and Helz, 2000). For the sake of  
401 showing the only predominating aqueous species, we removed the molybdenite from the  
402 calculations, and the results show that  $\text{MoS}_4^{2-}$  predominates when  $\text{pH} < 11$ , and mixed  
403  $\text{MoS}_4^{2-}/\text{MoO}_4^{2-}$  species in pH 11-12 (Fig. 10b), which is qualitatively consistent with previous  
404 studies and our experimental results, where no precipitation of molybdenite is observed in the  
405 experimental solutions. There are two possible explanations for the absence of molybdenite  
406 in the experimental solution: either slow precipitation of molybdenite precipitation is too  
407 slow to be observed, and/or uncertainties in the thermodynamic properties of molybdenite  
408 causing overestimation of its stability.

#### 409 4.2. Stability of thiomolybdate at high P-T

410 Our experimental results show that the thiomolybdate species with various ratios of  
411 sulfur and oxygen ligands are stable in our experimental solutions up to 330 °C. In the  
412 absence of experimental determination of thermodynamic properties for thiomolybdate  
413 species at elevated P-T conditions, it is useful to extrapolate the available data at ambient  
414 temperatures to elevated temperatures. The validity of these extrapolations can be evaluated

415 by comparison with the experimental EXAFS results, and the models can be used to assess  
416 the role of the thiomolybdates in transporting molybdenum in ore fluids.

417 [Erickson and Helz \(2000\)](#) determined the stability constants for  $(\text{MoO}_{4-x}\text{S}_x^{2-})$  in  $\text{H}_2\text{S}$ -  
418 bearing solutions at 25 °C. Based on their data, we used the isocoulombic approach ([Gu et  
419 al., 1994](#)) to extrapolate the formation constants of the  $\text{MoO}_{4-x}\text{S}_x^{2-}$  species up to 300 °C and  
420 water saturated pressure ([Table 5](#)).

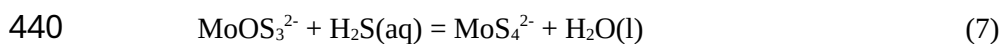
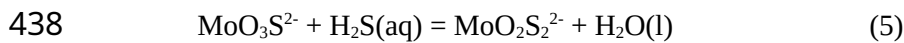
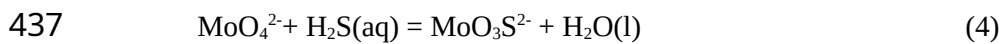
421 The basic assumption of the iso-coulombic extrapolation is that when a reaction has  
422 equal numbers of like-charged species on both sides of the reaction (iso-coulombic reaction),  
423 both heat capacity and entropy changes are small and tend to cancel one another, and the  
424 change of free energy is constant and independent of temperature ([Gu et al., 1994](#), [Liu et al.,  
425 2012](#)):

$$426 \quad DG_T^0 = DG_{T_r}^0 = -R \cdot T \cdot \ln K_T \quad (2)$$

427 where  $DG_{T_r}^0$  and  $DG_T^0$  refer to the standard Gibbs free energy ( $\text{J}\cdot\text{mol}^{-1}$ ) of reaction at reference  
428 temperature  $T_r$  (298.15 K) and the experimental temperature  $T$  (in Kelvin),  $R$  is the ideal gas  
429 constant ( $\text{J}\cdot\text{K}^{-1}\cdot\text{mol}^{-1}$ ) and  $K_T$  is the equilibrium constant for the iso-coulombic reaction.  
430 Therefore, the  $\log K$  for an iso-coulombic reaction at experimental temperature can be  
431 estimated from the  $\log K$  values at the reference temperature where the thermodynamic  
432 properties are available (e.g., [Liu et al., 2012](#)):

$$433 \quad \log K_T = \frac{T_r}{T} \log K_{T_r} \quad (3)$$

434 In the case of the thiomolybdate species, it is convenient that all the reactions of the  
435 replacement of  $\text{O}^{2-}$  by  $\text{S}^{2-}$  meet the requirement of iso-coulombic reactions, i.e., species on  
436 both sides of the reactions are equally charged:



441 Therefore, the stepwise formation constants for these species at elevated temperatures  
442 can be estimated with the room temperature data of [Erickson and Helz \(2000\)](#) using Eq. (3),  
443 and the results are compiled in [Table 5](#).



444 Based on the extrapolated data, the stability of the thiomolybdate and molybdate  
445 species were estimated as a function of pH and Eh at 300 °C in a solution with 0.1 m total  
446 sulfur (Fig. 10c). The thiomolybdate species, in particular  $\text{MoS}_4^{2-}$ , is predicted to be stable in  
447 the solution with slightly acidic to neutral pH (pH 6-8) under reduced conditions (sulfide  
448 stable), and molybdate species ( $\text{HMoO}_4^-$  and  $\text{MoO}_4^{2-}$ ) under more oxidised (sulfate stable),  
449 and acidic conditions (sulfide stable) (pH<6 at 300 °C),. Similar to the room temperature  
450 situation, our experimental results are qualitatively consistent with the extrapolation based on  
451 the room temperature data, i.e., mixed ligand species ( $\text{MoO}_3\text{S}^{2-}$  to  $\text{MoOS}_3^{2-}$ ) are present in the  
452 solution with pH values of 8.5-9, and  $\text{MoS}_4^{2-}$  would predominate in wide pH ranges (pH 5 -  
453 8.5 at 300 °C). Such pH range covers the major pH buffers in geological fluids, such as K-  
454 feldspar-Muscovite-Quartz (KMq),  $\text{H}_2\text{S}/\text{HS}^-$  and  $\text{CO}_{2(\text{aq})}/\text{HCO}_3^-$ , as shown in Fig. 10.

455 Therefore, both our experimental data and the extrapolations from room temperature  
456 thermodynamic properties indicate that the thiomolybdate species may contribute to Mo  
457 transport in hydrothermal sulfur-rich fluids with neutral to alkaline pH range under reduced  
458 conditions, and current models of Mo transport in hydrothermal ore fluids need to be re-  
459 evaluated to take into account the thiomolybdate species. It is notable that in very acidic  
460 solutions the molybdenite would precipitate in sulfide-stable solutions (Fig. 10c). Previous  
461 solubility study of Zhang et al. (2012) suggested  $\text{NaHMo}_2\text{S}_2$  as predominant Mo – S species  
462 but they found negative trend of molybdenite solubility with increasing  $\log f\text{S}_2$  at 600-800 °C  
463 and 2000 bar. Apart from the difference in the experimental temperatures and pressures  
464 between the two studies, their experimental solutions have pH range of 1-2 (measurement of  
465 quenched solutions, Zhang et al., 2012), which is too acidic to see the impact of  
466 thiomolybdate on the solubility of molybdenite, as indicate in Fig 10c. To this end, further  
467 experimental studies are needed to improve the thermodynamic properties for the  
468 thiomolybdate species at wide range of P-T conditions in order to accurately assess the role  
469 of thiomolybdate in transporting Mo (and possibility of transporting other metal ions such as  
470 Cu and Fe) in hydrothermal fluids. Finally, Our experiments show that Mo(VI) species  
471 predominate at high P-T in solutions with reduced sulfur, consistent with the previous studies  
472 in chloride solutions and vapours cited; therefore, Mo(VI) is likely to be the main oxidation  
473 state of molybdenum in typical hydrothermal ore fluids. Under extremely reduced conditions  
474 Mo(V) and/or Mo(IV) species may occur, but they are not considered due to a lack of  
475 experimental evidence and thermodynamic data for these species.

476

477 *Acknowledgement:* Research funding is from CSIRO and ARC. The EXAS measurements  
478 were conducted at the BM30B FAME beamline of the European Synchrotron Radiation  
479 Facility (ESRF), with travel funding from The International Synchrotron Access Program  
480 (ISAP) administered by the Australian Synchrotron. We thank Dr Peter Kappen and Dr  
481 Jeremy Wykes for helping in collect spectra of some standard compound at the XAS  
482 beamline of the Australian Synchrotron. The MD simulations were supported by the Pawsey  
483 Supercomputing Centre with funding from the Australian and Western Australian, and the  
484 National Computational Infrastructure (NCI) supported by the Australian Government.

## 485 5. References

- 486 Asael, D., Rouxel, O., Poulton, S.W., Lyons, T.W. and Bekker, A. (2018) Molybdenum  
487 record from black shales indicates oscillating atmospheric oxygen levels in the early  
488 Paleoproterozoic. *American Journal of Science* 318, 275-299.
- 489 Bankura, A., Karmakar, A., Carnevale, V., Chandra, A. and Klein, M.L. (2014) Structure,  
490 Dynamics, and Spectral Diffusion of Water from First-Principles Molecular  
491 Dynamics. *The Journal of Physical Chemistry C* 118, 29401-29411.
- 492 Becke, A.D. (1988) Density-functional exchange-energy approximation with correct  
493 asymptotic behavior. *Physical review. A, General physics* 38, 3098-3100.
- 494 Bernholc, J. and Stiefel, E.I. (1985) Electronic structure of thiomolybdates ( $\text{MoS}_4^{2-}$  and  
495  $\text{Mo}_3\text{S}_9^{2-}$ ). *Inorganic Chemistry* 24, 1323-1330.
- 496 Bethke, C.M. (2007) *Geochemical and Biogeochemical Reaction Modeling*, 2 ed. Cambridge  
497 University Press, Cambridge.
- 498 Bonnetti, C., Zhou, L., Riegler, T., Brugger, J. and Fairclough, M. (2020) Large S isotope and  
499 trace element fractionations in pyrite of uranium roll front systems result from  
500 internally-driven biogeochemical cycle. *Geochimica Cosmochimica Acta* 282, 113–  
501 132.
- 502 Borg, S., Liu, W.H., Etschmann, B., Tian, Y. and Brugger, J. (2012) An XAS study of  
503 molybdenum speciation in hydrothermal chloride solutions from 25-385 °C and  
504 600 bar. *Geochimica Et Cosmochimica Acta* 92, 292-307.

- 505 Bostick, B.C., Fendorf, S. and Helz, G.R. (2003) Differential Adsorption of Molybdate and  
506 Tetrathiomolybdate on Pyrite (FeS<sub>2</sub>). *Environmental Science & Technology* 37, 285-  
507 291.
- 508 Brugger, J., Etschmann, B., Liu, W., Testemale, D., Hazemann, J.L., Emerich, H., van Beek,  
509 W. and Proux, O. (2007) An XAS study of the structure and thermodynamics of Cu(I)  
510 chloride complexes in brines up to high temperature (400 °C, 600 bar). *Geochimica Et*  
511 *Cosmochimica Acta* 71, 4920-4941.
- 512 Brugger, J., Liu, W., Etschmann, B., Mei, Y., Sherman, D.M. and Testemale, D. (2016) A  
513 review of the coordination chemistry of hydrothermal systems: do coordination  
514 changes make ore deposits ? *Chemical Geology* 447, 219–253.
- 515 Bullock, L.A. and Parnell, J. (2017) Selenium and molybdenum enrichment in uranium roll-  
516 front deposits of Wyoming and Colorado, USA. *Journal of Geochemical Exploration*  
517 180, 101-112.
- 518 Candela, P.A. and Holland, H.D. (1984) The partitioning of copper and molybdenum  
519 between silicate melts and aqueous fluids. *Geochimica et Cosmochimica Acta* 48,  
520 373-3
- 521 Chantler, C.T. (1995) Theoretical Form Factor, Attenuation, and Scattering Tabulation for  
522 Z=1–92 from E=1–10 eV to E=0.4–1.0 MeV. *Journal of Physical and Chemical*  
523 *Reference Data* 24, 71-643.80.
- 524 Combariza, J.E., Enemark, J.H., Barfield, M. and Facelli, J.C. (1989) *Ab initio* molecular  
525 orbital studies of chemical shielding in transition-metal compounds: molybdenum-95  
526 shielding in molybdate and thiomolybdate [MoO<sub>n</sub>S<sub>(4-n)</sub>]<sup>2-</sup> anions. *J Am Chem Soc* 111,  
527 7619-7621.
- 528 Coucouvanis, D. (1998) Syntheses, Structures, and Reactions of Binary and Tertiary  
529 Thiomolybdate Complexes Containing the (O)Mo(S<sub>x</sub>) and (S)Mo(S<sub>x</sub>) Functional  
530 Groups (x = 1, 2, 4), in: Sykes, A.G. (Ed.), *Advances in Inorganic Chemistry*.  
531 Academic Press, pp. 1-73.
- 532 Dadze, T.P., Kashirtseva, G.A., Novikov, M.P. and Plyasunov, A.V. (2017) Solubility of  
533 MoO<sub>3</sub> in acid solutions and vapor-liquid distribution of molybdic acid. *Fluid Phase*  
534 *Equilibr* 440, 64-76.

- 535 Dadze, T.P., Kashirtseva, G.A., Novikov, M.P. and Plyasunov, A.V. (2018) Solubility of  
536 MoO<sub>3</sub> in Aqueous Acid Chloride-Bearing Solutions at 573 K. *Journal of Chemical &*  
537 *Engineering Data* 63, 1827-1832.
- 538 Dahl, T.W., Chappaz, A., Fitts, J.P. and Lyons, T.W. (2013) Molybdenum reduction in a  
539 sulfidic lake: Evidence from X-ray absorption fine-structure spectroscopy and  
540 implications for the Mo paleoproxy. *Geochimica et Cosmochimica Acta* 103, 213-  
541 231.
- 542 Driesner, T. and Heinrich, C.A. (2007) The system H<sub>2</sub>O–NaCl. Part I: Correlation formulae  
543 for phase relations in temperature–pressure–composition space from 0 to 1000 °C, 0  
544 to 5000 bar, and 0 to 1 X<sub>NaCl</sub>. *Geochimica et Cosmochimica Acta* 71, 4880-4901.
- 545 Driesner, T. (2007) The system H<sub>2</sub>O–NaCl. Part II: Correlations for molar volume, enthalpy,  
546 and isobaric heat capacity from 0 to 1000 °C, 1 to 5000 bar, and 0 to 1 X<sub>NaCl</sub>.  
547 *Geochimica et Cosmochimica Acta* 71, 4902-4919.
- 548 Ehrig, K., Mcphie, J. and Kamenetsky, V.S. (2012) Geology and mineralogical zonation of  
549 the Olympic Dam iron oxide Cu-U-Au-Ag deposit, South Australia. *Society of*  
550 *Economic Geologists, Special Publications* 16, 237–267.
- 551 El-Issa, B.D., Ali, A.A.M. and Zanati, H. (1989) Theoretical study of the bonding in sulfur-  
552 and oxygen-containing molybdenum species of the general formula MoSnO<sub>4-n</sub><sup>2-</sup> (n =  
553 0-4). *Inorganic Chemistry* 28, 3297-3305.
- 554 Erickson, B.E. and Helz, G.R. (2000) Molybdenum(VI) speciation in sulfidic waters::  
555 Stability and lability of thiomolybdates. *Geochimica et Cosmochimica Acta* 64, 1149-  
556 1158.
- 557 Etschmann, B.E., Liu, W., Testemale, D., Muller, H., Rae, N.A., Proux, O., Hazemann, J.L.  
558 and Brugger, J. (2010) An in situ XAS study of copper(I) transport as hydrosulfide  
559 complexes in hydrothermal solutions (25-592 °C, 180-600 bar): Speciation and  
560 solubility in vapor and liquid phases. *Geochimica Et Cosmochimica Acta* 74, 4723-  
561 4739.
- 562 Gillan, M.J., Alfè, D. and Michaelides, A. (2016) Perspective: How good is DFT for water?  
563 *The Journal of Chemical Physics* 144, 130901.
- 564 Goedecker, S., Teter, M. and Hutter, J. (1996) Separable dual-space Gaussian  
565 pseudopotentials. *Physical Review B* 54, 1703-1710.

- 566 Gu, Y., Gammons, C.H. and Bloom, M.S. (1994) A one-term extrapolation method for  
567 estimating equilibrium constants of aqueous reactions at elevated temperatures.  
568 *Geochimica et Cosmochimica Acta* 58, 3545-3560.
- 569 Guan, Q. Mei, Y., Etschmann, B., Testemale, D., Louvel, M. and Brugger, J. (2020) Yttrium  
570 complexation and hydration in chloride-rich hydrothermal fluids: a combined *ab initio*  
571 molecular dynamics and in situ X-ray absorption spectroscopy study. *Geochimica et*  
572 *Cosmochimica Acta* 281, 168-189.
- 573 Harmer, M.A. and Sykes, A.G. (1980) Kinetics of the interconversion of sulfido- and  
574 oxomolybdate(VI) species  $\text{MoO}_x\text{S}_{4-x}^{2-}$  in aqueous solutions. *Inorganic Chemistry* 19,  
575 2881-2885.
- 576 Hartwigsen, C., Goedecker, S. and Hutter, J. (1998) Relativistic separable dual-space  
577 Gaussian pseudopotentials from H to Rn. *Physical Review B* 58, 3641-3662.
- 578 Helz, G.R., Miller, C.V., Charnock, J.M., Mosselmans, J.F.W., Patrick, R.A.D., Garner, C.D.  
579 and Vaughan, D.J. (1996) Mechanism of molybdenum removal from the sea and its  
580 concentration in black shales: EXAFS evidence. *Geochimica et Cosmochimica Acta*  
581 60, 3631-3642.
- 582 Helz, G.R. and Erickson, B.E. (2011) Extraordinary stability of copper(I)-tetrathiomolybdate  
583 complexes: Possible implications for aquatic ecosystems. *Environmental Toxicology*  
584 *and Chemistry* 30, 97-102.
- 585 Helz, G.R., Erickson, B.E. and Vorlicek, T.P. (2014) Stabilities of thiomolybdate complexes  
586 of iron; implications for retention of essential trace elements (Fe, Cu, Mo) in sulfidic  
587 waters. *Metallomics* 6, 1131-1140.
- 588 Hoover, W.G. (1985) Canonical dynamics: Equilibrium phase-space distributions. *Physical*  
589 *Review A* 31, 1695-1697.
- 590 Humphrey, W., Dalke, A. and Schulten, K. (1996) VMD: visual molecular dynamics. *Journal*  
591 *of molecular graphics* 14, 33-38, 27-38.
- 592 Hurtig, N.C. and Williams-Jones, A.E. (2014) An experimental study of the transport of gold  
593 through hydration of AuCl in aqueous vapour and vapour-like fluids. *Geochimica et*  
594 *Cosmochimica Acta* 127, 305-325.

595 Hutter, J., Iannuzzi, M., Schiffmann, F. and VandeVondele, J. (2014) cp2k: atomistic  
596 simulations of condensed matter systems. WIREs Computational Molecular Science  
597 4, 15-25.

598 Jahn, S. and Schmidt, C. (2010) Speciation in Aqueous MgSO<sub>4</sub> Fluids at High Pressures and  
599 High Temperatures from *Ab Initio* Molecular Dynamics and Raman Spectroscopy.  
600 The Journal of Physical Chemistry B 114, 15565-15572.

601 Joly, Y. (2001) X-ray absorption near-edge structure calculations beyond the muffin-tin  
602 approximation. Phys. Rev. B 63, art. no.-125120.

603 Krause, M.O. and Oliver, J.H. (1979) Natural widths of atomic K and L levels, K<sub>α</sub> X-ray  
604 lines and several KLL Auger lines. Journal of Physical and Chemical Reference Data  
605 8, 329-338.

606 Keppler, H. and Wyllie, P.J. (1991) Partitioning of Cu, Sn, Mo, W, U, and Th between Melt  
607 and Aqueous Fluid in the Systems Haplogranite-H<sub>2</sub>O-HCl and Haplogranite-H<sub>2</sub>O-Hf.  
608 Contributions to Mineralogy and Petrology 109, 139-150.

609 Kudrin, A.V. (1989) Behavior of Mo in aqueous NaCl and KCl solutions at 300-450 °C.  
610 Geochem. Int. 26, 87-99.

611 Laurie, Stuart H. (2000) Thiomolybdates — Simple but Very Versatile Reagents. European  
612 Journal of Inorganic Chemistry 2000, 2443-2450.

613 Lee, C., Yang, W. and Parr, R.G. (1988) Development of the Colle-Salvetti correlation-  
614 energy formula into a functional of the electron density. Physical Review B 37, 785-  
615 789.

616 Lee, H.S. and Tuckerman, M.E. (2006) Structure of liquid water at ambient temperature from  
617 *ab initio* molecular dynamics performed in the complete basis set limit. The Journal of  
618 Chemical Physics 125, 154507.

619 Lin, I.C., Seitsonen, A.P., Tavernelli, I. and Rothlisberger, U. (2012) Structure and Dynamics  
620 of Liquid Water from *Ab Initio* Molecular Dynamics-Comparison of BLYP, PBE, and  
621 revPBE Density Functionals with and without van der Waals Corrections. Journal of  
622 chemical theory and computation 8, 3902-3910.

623 Liu, W., Brugger, J., Etschmann, B., Testemale, D. and Hazemann, J.-L. (2008) The  
624 solubility of nantokite (CuCl(s)) and Cu speciation in low density fluids near the

625 critical isochore: an in-situ XAS study. *Geochimica Et Cosmochimica Acta* 72, 4094–  
626 4106.

627 Liu, W., Borg, S., Testemale, D., Etschmann, B., Hazemann, J. and Brugger, J. (2011)  
628 Speciation and thermodynamic properties for cobalt chloride complexes in  
629 hydrothermal fluids at 35-440 °C and 600 bar: An in-situ XAS study. *Geochimica Et*  
630 *Cosmochimica Acta* 75, 1227-1248.

631 Liu, W., Borg, S., Etschmann, B., Mei, Y. and Brugger, J. (2012) An XAS study of  
632 speciation and thermodynamic properties of aqueous zinc bromide complexes at 25-  
633 150 °C. *Chemical Geology* 298, 57-69.

634 Liu, W., Etschmann, B., Testemale, D., Hazemann, J.-L., Rempel, K., Mueller, H. and  
635 Brugger, J. (2014) Gold transport in hydrothermal fluids: Competition among the Cl<sup>-</sup>,  
636 Br<sup>-</sup>, HS<sup>-</sup> and NH<sub>3</sub>(aq) ligands. *Chemical Geology* 376, 11-19.

637 Liu, X., Cheng, J., Sprik, M. and Lu, X. (2013a) Solution structures and acidity constants of  
638 molybdic acid. *Journal of Physical Chemistry Letters* 4, 2926-2930.

639 Liu, X., Sprik, M. and Cheng, J. (2013b) Hydration, acidity and metal complexing of  
640 polysulfide species: A first principles molecular dynamics study. *Chemical Physics*  
641 *Letters* 563, 9-14.

642 Mei, Y., Sherman, D.M., Liu, W. and Brugger, J. (2013) *Ab initio* molecular dynamics  
643 simulation and free energy exploration of copper(I) complexation by chloride and  
644 bisulfide in hydrothermal fluids. *Geochimica Et Cosmochimica Acta* 102, 45-64.

645 Mei, Y., Sherman, D., Liu, W. and Brugger, J. (2014) Metal complexation and ion hydration  
646 in low density hydrothermal fluids: *ab initio* molecular dynamics simulation of Cu(I)  
647 and Au(I) in chloride solutions (25-1000 °C, 1-5000 bar). *Geochimica et*  
648 *Cosmochimica Acta*, 131, 196–212.

649 Mei, Y., Etschmann, B., Liu, W., Sherman, D.M., Barnes, S.J., Fiorentini, M.L., Seward,  
650 T.M., Testemale, D. and Brugger, J. (2015) Palladium complexation in chloride- and  
651 bisulfide-rich fluids: Insights from *ab initio* molecular dynamics simulations and X-  
652 ray absorption spectroscopy. *Geochimica Et Cosmochimica Acta* 161, 128-145.

653 Mei, Y., Etschmann, B., Liu, W., Sherman, D.M., Testemale, D. and Brugger, J. (2016)  
654 Speciation and thermodynamic properties of zinc in sulfur-rich hydrothermal fluids:

655 Insights from *ab initio* molecular dynamics simulations and X-ray absorption  
656 spectroscopy. *Geochimica Et Cosmochimica Acta* 179, 32-52.

657 Mei, Y., Liu, W., Brugger, J., Sherman, D.M. (2018) The dissociation mechanism and  
658 thermodynamic properties of HCl(aq) in hydrothermal fluids (to 700 °C, 60 kbar) by  
659 *ab initio* molecular dynamics simulations. *Geochimica Cosmochimica Acta* 226, 84-  
660 106.

661 Mei, Y., Liu, W., Brugger, J., Guan, Q. (2020) Gold solubility in alkaline and ammonia-rich  
662 hydrothermal fluids: insights from *ab initio* molecular dynamics simulations.  
663 *Geochimica Cosmochimica Acta*. In press, <https://doi.org/10.1016/j.gca.2019.12.031>.

664 Minubayeva, Z. and Seward, T.M. (2010) Molybdic acid ionisation under hydrothermal  
665 conditions to 300 °C. *Geochimica Et Cosmochimica Acta* 74, 4365-4374.

666 Mosselmans, J.F.W., Patrick, R.A.D., Charnock, J.M. and Sole, V.A. (1999) EXAFS of  
667 copper in hydrosulfide solutions at very low concentrations: implications for the  
668 speciation of copper in natural waters. *Mineralogical Magazine* 63, 769-772.

669 Müller, A., Diemann, E., Jostes, R. and Bögge, H. (1981) Transition Metal Thiometalates:  
670 Properties and Significance in Complex and Bioinorganic Chemistry. *Angewandte*  
671 *Chemie International Edition in English* 20, 934-955.

672 Nosé, S. (1984) A unified formulation of the constant temperature molecular dynamics  
673 methods. *The Journal of Chemical Physics* 81, 511-519.

674 Pokrovski, G.S., Roux, J. and Harrichoury, J.C. (2005) Fluid density control on vapor-liquid  
675 partitioning of metals in hydrothermal systems. *Geology*, 33, 657-660.

676 Pokrovski, G.S., Tagirov, B.R., Schott, J., Hazemann, J.L. and Proux, O. (2009) A new view  
677 on gold speciation in sulfur-bearing hydrothermal fluids from in situ X-ray absorption  
678 spectroscopy and quantum-chemical modeling. *Geochimica et Cosmochimica Acta*  
679 73, 5406-5427.

680 Proux, O., Biquard, X., Lahera, E., Menthonnex, J.J., Prat, A., Ulrich, O., Soldo, Y.,  
681 Trevisson, P., Kapoujyan, G., Perroux, G., Taunier, P., Grand, D., Jeantet, P.,  
682 Deleglise, M., Roux, J.P. and Hazemann, J.L. (2005) FAME: A new beamline for X-  
683 ray absorption investigations of very-diluted systems of environmental, material and  
684 biological interests. *Physica Scripta* T115, 970-973.



685 Ravel, B. and Newville, M. (2005) ATHENA, ARTEMIS, HEPHAESTUS: data analysis for  
686 X-ray absorption spectroscopy using IFEFFIT. *J. Synchrot. Radiat.* 12, 537-541.

687 Rehr, J.J., Kas, J.J., Prange, M.P., Sorini, A.P., Takimoto, Y. and Vila, F. (2009) *Ab initio*  
688 theory and calculations of X-ray spectra. *Comptes Rendus Physique* 10, 548-559.

689 Rempel, K.U., Migdisov, A.A. and Williams-Jones, A.E. (2006) The solubility and speciation  
690 of molybdenum in water vapour at elevated temperatures and pressures: Implications  
691 for ore genesis. *Geochimica Et Cosmochimica Acta* 70, 687-696.

692 Rempel, K.U., Williams-Jones, A.E. and Migdisov, A.A. (2008) The solubility of  
693 molybdenum dioxide and trioxide in HCl-bearing water vapour at 350 °C and  
694 pressures up to 160 bars. *Geochimica et Cosmochimica Acta* 72, 3074-3083.

695 Rempel, K.U., Williams-Jones, A.E. and Migdisov, A.A. (2009) The partitioning of  
696 molybdenum(VI) between aqueous liquid and vapour at temperatures up to 370 °C.  
697 *Geochimica et Cosmochimica Acta* 73, 3381-3392.

698 Robie, R.A. and Hemingway, B.S. (1995) Thermodynamic properties of minerals and related  
699 substances at 298.15 K and 1 bar ( $10^5$  Pascals) pressure and at higher temperatures.  
700 US Geological Survey Bulletin 2131, 461.

701 Smedley, P.L. and Kinniburgh, D.G. (2017) Molybdenum in natural waters: A review of  
702 occurrence, distributions and controls. *Appl Geochem* 84, 387-432.

703 Pokrovski, G.S., Tagirov, B.R., Schott, J., Hazemann, J.L. and Proux, O. (2009) A new view  
704 on gold speciation in sulfur-bearing hydrothermal fluids from in situ X-ray absorption  
705 spectroscopy and quantum-chemical modeling. *Geochimica Et Cosmochimica Acta*  
706 73, 5406-5427.

707 Rempel, K.U., Migdisov, A.A. and Williams-Jones, A.E. (2006) The solubility and speciation  
708 of molybdenum in water vapour at elevated temperatures and pressures: Implications  
709 for ore genesis. *Geochimica Et Cosmochimica Acta* 70, 687-696.

710 Rempel, K.U., Williams-Jones, A.E. and Migdisov, A.A. (2008) The solubility of  
711 molybdenum dioxide and trioxide in HCl-bearing water vapour at 350 °C and  
712 pressures up to 160 bars. *Geochimica et Cosmochimica Acta* 72, 3074-3083.

713 Rempel, K.U., Williams-Jones, A.E. and Migdisov, A.A. (2009) The partitioning of  
714 molybdenum (VI) between aqueous liquid and vapour at temperatures up to 370 °C.  
715 *Geochimica et Cosmochimica Acta* 73, 3381-3392.

- 716 Saha, P., Anderson, A.J., Lee, T. and Klemm, M. (2017) The Solubility of Tugarinovite  
717 (MoO<sub>2</sub>) in H<sub>2</sub>O at Elevated Temperatures and Pressures. *Geofluids* 2017, 12.
- 718 Seedorff, E., Dilles, J.H., Proffett, J.M., Jr., Einaudi, M.T., Zurcher, L., Stavast, W.J.A.,  
719 Johnson, D.A., Barton, M.D., Hedenquist, J.W., Thompson, J.F.H., Goldfarb, R.J. and  
720 Richards, J.P. (2005) Porphyry Deposits: Characteristics and Origin of Hypogene  
721 Features, One Hundredth Anniversary Volume. Society of Economic Geologists, p. 0.
- 722 Stefanski, J. and Jahn, S. (2020) Yttrium speciation in subduction zone fluids from *ab initio*  
723 molecular dynamics simulations. *Solid Earth Discuss.* 2020, 1-36.
- 724 Sulpizi, M., Salanne, M., Sprik, M. and Gaigeot, M.-P. (2013) Vibrational Sum Frequency  
725 Generation Spectroscopy of the Water Liquid–Vapor Interface from Density  
726 Functional Theory-Based Molecular Dynamics Simulations. *The Journal of Physical*  
727 *Chemistry Letters* 4, 83-87.
- 728 Tessin, A., Chappaz, A., Hendy, I. and Sheldon, N. (2018) Molybdenum speciation as a  
729 paleo-redox proxy: A case study from late cretaceous western interior seaway black  
730 shales. *Geology* 47, 59-62
- 731 Testemale, D., Argoud, R., Geaymond, O. and Hazemann, J.L. (2005) High pressure high  
732 temperature cell for x-ray absorption and scattering techniques. *Rev. Sci. Instrum.* 76,  
733 043905.
- 734 Testemale, D., Brugger, J., Liu, W., Etschmann, B. and Hazemann, J.-L. (2009) In-situ X-ray  
735 absorption study of Iron(II) speciation in brines up to supercritical conditions.  
736 *Chemical Geology* 264, 295-310.
- 737 Tooth, B., Etschmann, B., Pokrovski, G.S., Testemale, D., Hazemann, J.L., Grundler, P.V.  
738 and Brugger, J. (2013) Bismuth speciation in hydrothermal fluids: An x-ray  
739 absorption spectroscopy and solubility study. *Geochimica et Cosmochimica Acta*, 101  
740 156-172.
- 741 Tossell, J.A. (2005) Calculation of the UV-visible spectra and the stability of Mo and Re  
742 oxysulfides in aqueous solution. *Geochimica et Cosmochimica Acta* 69, 2497-2503.
- 743 Ulrich, T. and Mavrogenes, J. (2008) An experimental study of the solubility of molybdenum  
744 in H<sub>2</sub>O and KCl-H<sub>2</sub>O solutions from 500 °C to 800 °C, and 150 to 300 MPa.  
745 *Geochimica et Cosmochimica Acta* 72, 2316-2330.

746 VandeVondele, J. and Hutter, J. (2007) Gaussian basis sets for accurate calculations on  
747 molecular systems in gas and condensed phases. *The Journal of Chemical Physics*  
748 127, 114105.

749 Wagner, J., Haigis, V., Künzel, D. and Jahn, S. (2017) Trace element partitioning between  
750 silicate melts – A molecular dynamics approach. *Geochimica et Cosmochimica Acta*  
751 205, 245-255.

752 Wood, S.A., Crerar, D.A. and Borcsik, M.P. (1987) Solubility of the assemblage pyrite-  
753 pyrrhotite-magnetite-sphalerite-galena-gold-stibnite-bismuthinite-argen- tite-  
754 molybdenite in H<sub>2</sub>O-NaCl-CO<sub>2</sub> solutions from 200 to 350 °C degrees. *Economic*  
755 *Geology* 82, 1864-1887.

756 Zajacz, Z., Candela, P.A. and Piccoli, P.M. (2017) The partitioning of Cu, Au and Mo  
757 between liquid and vapor at magmatic temperatures and its implications for the  
758 genesis of magmatic-hydrothermal ore deposits. *Geochimica et Cosmochimica Acta*  
759 207, 81-101.

760 Zhang, N., Yi, H., Zeng, D., Zhao, Z., Wang, W. and Costanzo, F. (2018) Structure evolution  
761 of mononuclear tungsten and molybdenum species in the protonation process: Insight  
762 from FPMD and DFT calculations. *Chemical Physics* 502, 77-86.

763

764 Table 1 Sample compositions. pH values are calculated from the compositions of NaHS,  
 765 Na<sub>2</sub>MoO<sub>4</sub> and NaCl using HCh modelling package and the default database (Shvarov, 2008).

Solution	Composition (m: mole/kg)	T (°C)	pH (30 °C, 800 bar)	pH (286°C, 800 bar)
Sol 5	0.004 m Na <sub>2</sub> MoO <sub>4</sub> , 1.13 m NaHS	30, 103, 194, 286	11.5	8.5
Sol 6	0.006 m Na <sub>2</sub> MoO <sub>4</sub> , 2.00 m NaHS	30, 103, 194, 286	11.4	8.5
Sol 8	0.008 m Na <sub>2</sub> MoO <sub>4</sub> , 0.28 m NaHS	30, 103, 194, 286, 370, 394	11.9	8.8
Sol 10	0.009 m Na <sub>2</sub> MoO <sub>4</sub> , 0.28 m NaHS, 1.0 m NaCl	30, 103, 194, 286, 330	11.8	8.7
Sol 12	0.009 m Na <sub>2</sub> MoO <sub>4</sub> , 0.070 m NaHS	30, 103, 194, 286, 330, 370	11.8	8.6
Sol 14	0.009 m Na <sub>2</sub> MoO <sub>4</sub> , 0.04 m NaHS	30, 103, 194, 286, 330, 370	12.0	8.8
Sol 15	0.007 m Na <sub>2</sub> MoO <sub>4</sub> , 0.43 m NaHS	30, 103, 194, 286, 330, 370, 394	11.8	8.7

766

767 Table 2. Details of ab initio MD simulation using CP2K.

solution composition	Job ID	T (°C)	P (bar)	Density of box (g/cm <sup>3</sup> )	Box size (Å)
1 H <sub>2</sub> MoO <sub>4</sub> , 4 Na <sup>+</sup> , 4 HS <sup>-</sup> , 111 H <sub>2</sub> O	1	77	800	1.1114 6	15.277
	2	200	20	0.9911	15.872
	3	200	800	1.0291 5	15.674
	4	300	100	0.8844	16.486
	5	300	800	0.9421 6	16.142
1 MoO <sub>4</sub> <sup>2-</sup> , 2 Na <sup>+</sup> , 111 H <sub>2</sub> O	6	77	800	1.0740	15.053
	7	200	800	0.9859	15.489
	8	300	800	0.8887	16.034
1 MoO <sub>4</sub> <sup>2-</sup> , 4Na <sup>+</sup> , 2HS <sup>-</sup> , 111 H <sub>2</sub> O	9	77	800	1.1039	15.165
	10	200	800	1.0183	15.578
	11	300	800	0.9260	16.079

768

769

770  
771  
772

Table 3 EXAFS refinement (nO and nS; number of oxygen and sulfur ligands; rO and rS: Mo-O and Mo-S bond distances,  $n_{\text{tot}}$ : number of total ligands;  $\sigma^2$ : Debye-waller factor; E0: shift of energy;  $\chi^2_{\text{red}}$ : reduced  $\chi^2$ , R-factor: goodness of fit. Fitting range in R space: 1-3 (Å)).

.T	nO	rO (Å)	nS	rS (Å)	$\sigma^2$	E0	$\chi^2_{\text{red}}$	R-factor	k-range
<b>Sol 14 0.04 m HS-</b>									
30	3.8(1)	1.766(5)	0.2(1)	2.276 (fix)	0.002(1)	6.6(6)	128	0.016	3-11
103	3.8(1)	1.769(5)	0.2(1)	2.276 (fix)	0.002(1)				3-11
194	3.3(2)	1.760(6)	0.7(2)	2.29(2)	0.002(1)				3-11
286	3.4(1)	1.758(5)	0.6(1)	2.28(2)	0.002(1)				3-11
330	3.8(1)	1.764(5)	0.2(1)	2.31(8)	0.002(1)				
330	4.0(2)	1.763 (fix)	0.0(2)		0.0029(8)	2.2(9)			3-11
<b>Sol 12 0.07 m HS-</b>									
30	3.3(2)	1.763(9)	0.7(2)	2.276 (fix)	0.002(1)	6.0(7)	221	0.031	3-11
103	3.4(2)	1.765(6)	0.6(2)	2.266 (fix)	0.002(1)				3-11
194	3.2(1)	1.763(6)	0.8(1)	2.286 (fix)	0.004(1)				3-11
286	3.3(2)	1.768(6)	0.7(2)	2.286 (fix)	0.003(1)				3-11
330	3.5(2)	1.767(8)	0.5(2)	2.286 (6)	0.003(1)				3-11
<b>Sol 8 0.28 m HS-</b>									
30	3.0(1)	1.76(2)	1.0(1)	2.24(3)	0.002(1)	1(2)	431	0.038	3-8.5
103	2.7(3)	1.75(1)	1.3(3)	2.24(2)	0.002(1)	5(2)			3-12
194	2.8(3)	1.75(1)	1.2(3)	2.25(2)	0.002(1)	5(2)			3-12
286	3.1(2)	1.75(1)	0.9(2)	2.27(3)	0.003(1)	5(2)			3-12
<b>Sol 10 0.28 m HS- + 1 m NaCl</b>									
30	2.6(2)	1.760(9)	1.4(2)	2.26(1)	0.0023(8)	4(1)	281	0.042	3-11

103	2.5(2)	1.760(9)	1.5(2)	2.27(1)	0.0026(8)				3-11
194	2.4(3)	1.75(2)	1.6(3)	2.27(2)	0.003(2)				3-10
286	2.8(2)	1.750(9)	1.2(2)	2.28(2)	0.0025(9)				3-11
330	3.0(2)	1.75(1)	1.0(2)	2.28(3)	0.003(1)	6(2)			3-11

---

**Sol 15 0.43 m HS-**

30	2.4(2)	1.75(1)	1.6(2)	2.25(1)	0.002(1)	5.2(7)	153	0.024	3-11
103	2.3(1)	1.746(6)	1.7(1)	2.239(7)	0.0014(5)				3-11
194	2.6(2)	1.741(8)	1.4(2)	2.25(1)	0.002(1)				3-11
286	2.9(2)	1.747(7)	1.1(2)	2.26(1)	0.002(2)				3-11
330	3.1(2)	1.750(7)	0.9(2)	2.26(2)	0.002(1)				3-10

---

**Sol 5 1.1 m HS-**

30	1.0(1)	1.688 (fix)	3.0(1)	2.211(5)	0.0025(5)	6.4(5)	171	0.018	3-10
103	0.4(1)	1.668 (fix)	3.6(1)	2.206(4)	0.0017(4)				3-11
194	1.0(2)	1.738 (fix)	3.0(2)	2.212(7)	0.0025(9)				3-11
286	2.4(2)	1.748(9)	1.6(2)	2.26(1)	0.0035(9)				3-11

---

**Sol 6 2 m HS-**

30	0.9(1)	1.708 (fix)	3.1(1)	2.210(5)	0.0015(6)	6.1(4)	157	0.016	3-12
103	0.7(2)	1.718 (fix)	3.3(2)	2.210(5)	0.0018(6)				3-12
194	0.6(1)	1.738 (fix)	3.4(1)	2.212(4)	0.0021(5)				3-12
286	1.7(1)	1.738 (fix)	2.3(1)	2.229(6)	0.0032(6)				3-11

773

774

775

776 Table 4. Simulation results of molybdate and thiomolybdate species.

Initial configuration of Mo	Job ID	T (°C)	P bar	MD time (ps)	species	Species time (ps)	Mo-S			Mo-O		
							CN	R (Å)	$\sigma_s^2$ (Å <sup>2</sup> )	CN	R (Å)	$\sigma_o^2$ (Å <sup>2</sup> )
H <sub>2</sub> MoO <sub>4</sub>	1A	77	800	13.64	H <sub>2</sub> MoO <sub>4</sub> & HMoO <sub>4</sub> <sup>-</sup>	12.64	0	-	-	4	1.81(4)	0.0057
	2A	200	20	15.55	HMoO <sub>4</sub> <sup>-</sup>	14.05	0	-	-	3(O) 1(OH)	1.77(4) 1.93(4)	0.0014 0.0019
	3A	200	800	10.30	HMoO <sub>4</sub> <sup>-</sup>	9.30	0	-	-	3(O) 1(OH)	1.77(4) 1.92(5)	0.0013 0.0021
	4A	300	100	13.49	HMoO <sub>4</sub> <sup>-</sup> & MoO <sub>4</sub> <sup>2-</sup>	11.99	0	-	-	4	1.81(5)	0.0058
	5A	300	800	10.17	HMoO <sub>4</sub> <sup>-</sup>	9.17	0	-	-	3(O) 1(OH)	1.77(3) 1.92(5)	0.0012 0.0027
MoO <sub>3</sub> S <sup>2-</sup>	1B	77	800	10.16	MoO <sub>3</sub> S <sup>2-</sup>	9.16	1	2.25(5)	0.0026	3	1.79(3)	0.0011
	2B	200	20	11.13	MoO <sub>3</sub> S <sup>2-</sup>	10.13	1	2.27(6)	0.0031	3	1.79(4)	0.0013
	3B	200	800	10.39	MoO <sub>3</sub> S <sup>2-</sup>	9.39	1	2.27(5)	0.0025	3	1.79(4)	0.0017
	4B	300	100	10.02	MoO <sub>3</sub> S <sup>2-</sup>	9.02	1	2.27(6)	0.0031	3	1.79(4)	0.0020
	5B	300	800	10.45	MoO <sub>3</sub> S <sup>2-</sup>	9.45	1	2.28(6)	0.0036	3	1.79(4)	0.0018
MoO <sub>2</sub> S <sub>2</sub> <sup>2-</sup>	1C	77	800	10.07	MoO <sub>2</sub> S <sub>2</sub> <sup>2-</sup>	9.07	2	2.24(4)	0.0017	2	1.79(3)	0.0011
	2C	200	20	9.51	MoO <sub>2</sub> S <sub>2</sub> <sup>2-</sup>	8.51	2	2.27(5)	0.0030	2	1.78(3)	0.0012
	3C	200	800	10.20	MoO <sub>2</sub> S <sub>2</sub> <sup>2-</sup>	9.20	2	2.25(6)	0.0030	2	1.79(4)	0.0014
	4C	300	100	10.02	MoO <sub>2</sub> S <sub>2</sub> <sup>2-</sup>	9.02	2	2.26(6)	0.0036	2	1.79(4)	0.0020
	5C	300	800	10.38	MoO <sub>2</sub> S <sub>2</sub> <sup>2-</sup>	9.38	2	2.26(6)	0.0038	2	1.78(4)	0.0017
MoOS <sub>3</sub> <sup>2-</sup>	1D	77	800	10.55	MoOS <sub>3</sub> <sup>2-</sup>	9.55	3	2.23(4)	0.0016	1	1.78(3)	0.0009
	2D	200	20	9.23	MoOS <sub>3</sub> <sup>2-</sup>	8.23	3	2.24(6)	0.0033	1	1.78(4)	0.0014
	3D	200	800	10.02	MoOS <sub>3</sub> <sup>2-</sup>	9.02	3	2.24(5)	0.0023	1	1.78(4)	0.0013
	4D	300	100	9.89	MoOS <sub>3</sub> <sup>2-</sup>	11.02	3	2.25(6)	0.0034	1	1.77(4)	0.0017
	5D	300	800	10.54	MoOS <sub>3</sub> <sup>2-</sup>	9.54	3	2.25(6)	0.0037	1	1.78(4)	0.0014
MoS <sub>4</sub> <sup>2-</sup>	1E	77	800	10.51	MoS <sub>4</sub> <sup>2-</sup>	9.51	4	2.23(5)	0.0024	0	-	-
	2E	200	20	10.21	MoS <sub>4</sub> <sup>2-</sup>	9.21	4	2.23(5)	0.0024	0	-	-
	3E	200	800	10.26	MoS <sub>4</sub> <sup>2-</sup>	9.26	4	2.23(5)	0.0027	0	-	-
	4E	300	100	9.90	MoS <sub>4</sub> <sup>2-</sup>	8.90	4	2.23(6)	0.0031	0	-	-
	5E	300	800	10.63	MoS <sub>4</sub> <sup>2-</sup>	9.63	4	2.23(6)	0.0033	0	-	-
MoO <sub>4</sub> <sup>2-</sup>	6	77	800	17.73	MoO <sub>4</sub> <sup>2-</sup>	16.73	-	-	-	4	1.80(3)	0.0011
	7	200	800	24.89	MoO <sub>4</sub> <sup>2-</sup>	23.89	-	-	-	4	1.80(4)	0.0016
	8	300	800	15.48	MoO <sub>4</sub> <sup>2-</sup>	14.48	-	-	-	4	1.81(4)	0.0018
MoO <sub>4</sub> <sup>2-</sup>	9	77	800	14.78	MoO <sub>4</sub> <sup>2-</sup>	13.78	-	-	-	4	1.80(3)	0.0011
	10	200	800	13.04	MoO <sub>4</sub> <sup>2-</sup>	12.04	-	-	-	4	1.80(4)	0.0017
	11	300	800	10.37	HMoO <sub>4</sub> <sup>-</sup>	9.37	-	-	-	3(O) 1(OH)	1.77(3) 1.94(5)	0.0012 0.0025

778 Table 5 The stepwise formation constants for thiomolybdate species extrapolated from  
 779 [Erickson and Helz \(2000\)](#).

Temperature (°C)	0	25	60	100	150	200	250	300
$\text{MoO}_4^{2-} + \text{H}_2\text{S}(\text{aq}) = \text{MoO}_3\text{S}^{2-} + \text{H}_2\text{O}(\text{l})$	5.67	5.19	4.64	4.15	3.66	3.27	2.96	2.70
$\text{MoO}_3\text{S}^{2-} + \text{H}_2\text{S}(\text{aq}) = \text{MoO}_2\text{S}_2^{2-} + \text{H}_2\text{O}(\text{l})$	5.24	4.80	4.30	3.84	3.38	3.02	2.74	2.50
$\text{MoO}_2\text{S}_2^{2-} + \text{H}_2\text{S}(\text{aq}) = \text{MoOS}_3^{2-} + \text{H}_2\text{O}(\text{l})$	5.46	5.00	4.47	4.00	3.52	3.15	2.85	2.60
$\text{MoOS}_3^{2-} + \text{H}_2\text{S}(\text{aq}) = \text{MoS}_4^{2-} + \text{H}_2\text{O}(\text{l})$	5.33	4.88	4.37	3.90	3.44	3.08	2.78	2.54

780

781



## 782 Figure captions

783 Fig. 1. Molybdenum K-edge XANES spectra as a function of NaHS concentration at 30 °C  
784 (a) and 286 °C (b). Dotted lines in (a) represent standard structures: Also shown in (a)  
785 are the measured spectra of  $[\text{MoO}_4]^{2-}$  moiety in  $\text{Na}_2\text{MoO}_4(\text{solid})$ , and  $[\text{MoS}_4]^{2-}$  in  
786  $(\text{NH}_4)_2\text{MoS}_4(\text{solid})$ .

787 Fig. 2. Evolution of the XANES spectra for all sample solutions as a function of temperature,  
788 from 30 °C (blue line) to the maximum experimental temperature as labelled (red  
789 line). The temperature increments for each sample are listed in Table 1.

790 Fig. 3. Fourier transforms of the EXAFS spectra at 30 °C (a) and 286 °C (b). The solid lines  
791 are measured data and dashed lines are the fits using the parameters listed in the  
792 Table 3. Also shown in (a) are the spectra of  $[\text{MoO}_4]^{2-}$  moiety in  $\text{Na}_2\text{MoO}_4(\text{solid})$ , and  
793  $[\text{MoS}_4]^{2-}$  in  $(\text{NH}_4)_2\text{MoS}_4(\text{solid})$ .

794 Fig. 4. Molybdenum K-edge EXAFS spectra in K-space (a) and Fourier transforms of  
795 EXAFS (b) collected at 30 °C to the maximum temperature as labelled for all sample  
796 solutions. The solid lines are measured data, and dashed lines are the fits using the  
797 parameters listed in Table 3. The composition and temperature increment for each  
798 sample are listed in Table 1.

799 Fig. 5. The change of ligand number derived from the EXAFS refinement as a function of  
800 NaHS concentration at 30 °C (a) and 286 °C (b) and 800 bar.

801 Fig. 6. Snapshots of hydrogen molybdate ions and molybdate species, determined from the  
802 MD simulations.

803 Fig. 7. Radial distribution function (RDF; solid lines) and coordination number (CN; dashed  
804 lines) for simulation 5A, 5B, 5C, 5D, 5E and 8.

805 Fig. 8. Snapshots of thiomolybdates determined from the MD simulations (bond distances see  
806 Table 3).

807 Fig. 9. The calculated XANES spectra using FDMNES and select experimental spectra. The  
808 XANES calculations are based on the molecular dynamic simulations of the structures  
809 for the species (see legend) at 77 and 300 °C. The Molybdenum K-edge (20,000 eV)  
810 was subtracted from the experimental energy for the x-axis of experimental spectra.  
811 The  $[\text{MoO}_4]^{2-}$  standard is  $\text{Na}_2\text{MoO}_4$  and  $[\text{MoS}_4]^{2-}$  is  $(\text{NH}_4)_2\text{MoS}_4$  solids.

812 Fig. 10. Predominant Mo species in sulfur-bearing solutions (total Mo = 1 ppm, total sulfur =  
813 0.1 m) as a function of pH and oxygen fugacity at 25 (a, b) and 300 °C (c, d). The  
814 calculations are done using The Geochemist's Workbench (Bethke, 2007) and the  
815 default thermodynamic database. The presence of molybdenite is suppressed in (b)  
816 and (d) to show only the fields of aqueous Mo(VI) species, The solubility contour of  
817 molybdenite of 10 and 100 ppb are also shown in (c). Blue dashed lines show the  
818 boundaries between stability fields of sulfur species, and the greyed areas show the  
819 estimated pH ranges of the experimental solutions (Table 1). Also shown in Fig c and  
820 d are the positions of the pH buffers of  $\text{CO}_2(\text{aq})/\text{HCO}_3^-$  and K-feldspar-Quartz-  
821 Muscovite (KMq,  $a_{\text{K}^+} = 0.1$ ).

822

823

824

825

826